AUTHOR(S):

TITLE:

YEAR:

Publisher citation:

OpenAIR citation:

Publisher copyright statement:

This is the _____ version of an article originally published by _____ in _____ (ISSN _____; eISSN _____).

Achieving High Strength and Ductility in Magnesium Alloys via Densely Hierarchical Double Contraction Nanotwins

Hui Fu,[†] Bincheng Ge,[†] Yunchang Xin,[‡] Ruizhi Wu,[§] Carlos Fernandez,[∥] Jianyu Huang,[†] and Qiuming Peng*,[†]

[†]State Key Laboratory of Metastable Materials Science and Technology, Yanshan University, Qinhuangdao 066004, China

[‡]School of Materials Science and Engineering, Chongqing University, Chongqing, 400044, P. R. China

[§]Key Laboratory of Superlight Materials & Surface Technology, Ministry of Education, Harbin Engineering University, Harbin, 150001, P. R. China

[∥]School of Pharmacy and Life Sciences, Rober Gordon University, Aberdeen, AB107GJ, United Kingdom

Ⓢ Supporting Information

ABSTRACT: Light-weight magnesium alloys with high strength are especially desirable for the applications in transportation, aerospace, electronic components, and implants owing to their high stiffness, abundant raw materials, and environmental friendliness. Unfortunately, conventional strengthening methods mainly involve the formation of internal defects, in which particles and grain boundaries prohibit dislocation motion as well as compromise ductility invariably. Herein, we report a novel strategy for simultaneously achieving high specific yield strength ($\sim$160 kN m kg^{-1}) and good elongation ($\sim$23.6%) in a duplex magnesium alloy containing 8 wt % lithium at room temperature, based on the introduction of densely hierarchical $\{10\bar{1}1\}-\{10\bar{1}1\}$ double contraction nanotwins (DCTWs) and full-coherent hexagonal close-packed (hcp) particles in twin boundaries by ultrahigh pressure technique. These hierarchical nanoscaled DCTWs with stable interface characteristics not only bestow a large fraction of twin interface but also form interlaced continuous grids, hindering possible dislocation motions. Meanwhile, orderly aggregated particles offer supplemental pinning effect for overcoming latent softening roles of twin interface movement and detwinning process. The processes lead to a concomitant but unusual situation where double contraction twinning strengthens rather than weakens magnesium alloys. Those cutting-edge results provide underlying insights toward designing alternative and more innovative hcp-type structural materials with superior mechanical properties.

KEYWORDS: Nanotwins, double contraction twinning, ultrahigh pressure, Mg−Li alloy
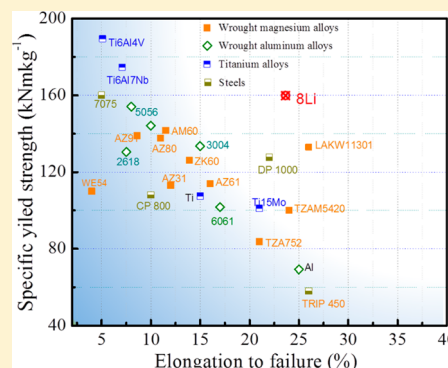
With regards to environmental protection and sustainable development, lightweight magnesium (Mg) alloys have attracted much attention as alternative metals for traditional structural materials.[1] Although they possess high specific-strength and great castability, there are, however, two critical bottlenecks, impeding their applications as potential structural materials which are relatively low strength and limited cold workability at room temperature.[2] The strength has been significantly improved in the past decades in the light of alloying,[3] grain refining,[4] composites,[5] and thermal-mechanical treatment.[6] In contrast, due to limited slip systems of the hcp-type crystal structure during deformation, the deformability of Mg alloys is inevitably related to the formation and growth of twins. Consequently, the crucial issue to enhance formability and mechanical properties of Mg alloys mostly focuses on twin varieties and their related deformation mechanisms.

Analogous to grain boundaries (GBs), interfaces of twin boundaries (TBs) play an important role in tailoring mechanical properties through dislocation interactions with internal barriers.[7−9] Moreover, compared with traditional high-angle GBs, TBs usually exhibit much higher thermal and mechanical stability.[9] The aggregation of alloying elements or impurities in these twin interfaces remarkably reduces elastic strain energies.[10] In this regard, twinning strength is deemed as a possible mechanism in high-performance Mg alloys, akin to grain refining strengthening and precipitation hardening.[11] However, although strengthening of TBs is quantitatively similar to that of GBs, strengthening from coherent TBs is relatively less pronounced than that from grain refinement when TB spacing is of micrometer scale. Therefore, to date, the preparation of high-density stable TBs is a technical challenge in the processing field of Mg alloys.[12]

Principally, the most common observed twin modes in Mg alloys are $\{10\bar{1}2\}$ tension twins (TTWs) and $\{10\bar{1}1\}$ contraction twins (CTWs).[13,14] The former is activated to accommodate tension strain along the c-axis.[15] The latter
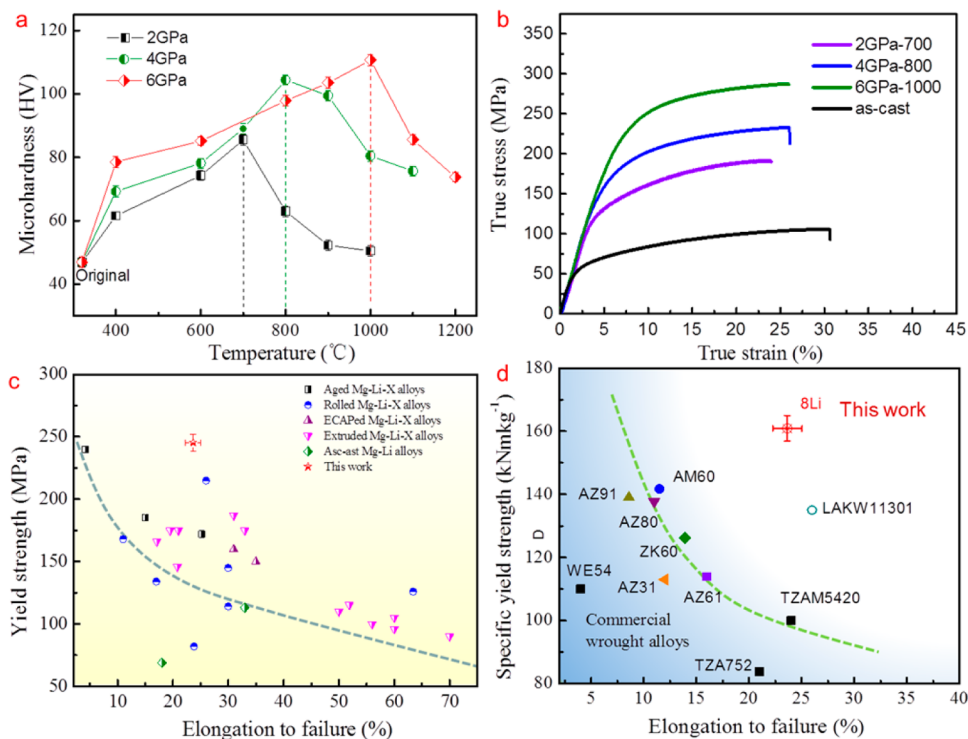
Figure 1. Mechanical properties of Mg−8Li alloys. Microhardness (a) and tensile curves (b) of Mg−8Li alloys prepared under different conditions. (c) Yield strength and elongation to failure of various Mg−Li alloys and Mg−Li−X alloys (X: alloying elements) by different fabrication techniques, such as rolling,[24] extrusion,[25−27] ECAP,[28,29] and aging.[30,31] (d) Comparison of specific yield strength between UHP Mg−8Li alloy and typical commercial Mg alloys.

corresponds to compression strain in the direction of *c*-axis.[16] The interface of TTWs is unstable and moves forward, even occupying whole grain during deformation. Hence, the spacing of TTWs often remains in a range of several to ten microns.[14] CTWs, on the other hand, remains fine and sometimes nucleates a secondary tension twin inside their domain,[17] resulting in the occurrence of $\{10\bar{1}1\}-\{10\bar{1}2\}$ double twins (DTWs).[18] However, owing to unstable interface characteristic of TTWs, this secondary tension twin would grow to fill entire CTWs during deformation, obstructing the reduction of twin spacing. Finally, the stress localization aggregates in the vicinity of twin−twin junction interfaces, resulting in the premature failure.[19]

Intuitively, it is expected that the avoidance or suppression of CTWs and DTWs by means of alloying or grain size reduction will improve ductility.[19] A presumption in Mg alloys that it until now was thought impossible to achieve high strength-ductility by twin mechanism, dissimilar to Cu or Ni alloys.[20] In fact, plastic relaxation of stress concentrations that occur at DTWs boundaries or twin tips is limited due to the most difficult ratio of $\langle c + a \rangle$ slip in contrast to $\langle a \rangle$ basal slip (in the range of 12−15).[21] Therefore, voids and cracks are prone to form near to DTWs. It does suggest that it is not the deformation twins themselves that cause failure but the lack of plastic relaxation.[18] Providing that some new and stable twins will be prepared by tuning local effects within the interior of grains, in which plastic deformation modes are easily available to relieve stress concentrations, a high-strength ductility Mg alloy would be expected.

Herein, a novel strengthening strategy of $\{10\bar{1}1\}-\{10\bar{1}1\}$ double contraction twins (DCTWs) has been successfully prepared to achieve high strength-ductility in Mg−Li alloys. To

the best of our knowledge, this is the first report in which the microhardness and yield strength of Mg−Li alloys are sharply improved without obvious losing ductility. To achieve this unique structure, three crucial requisites were considered. (1) A duplex Mg−8 wt % Li (simplified as Mg−8Li in the following section) alloy was selected as a representative system to test this conception, in which the $\langle c + a \rangle$ slip is closer to $\langle a \rangle$ basal slip,[22] and then it is possible to attain new twins. (2) A structure of DCTWs was employed rather than $\{10\bar{1}2\}-\{10\bar{1}2\}$ double tension twins (DTTWs),[18] wherein the interface of CTWs is more stable and the width is smaller in contrast to those of TTWs. Hence, the axis-direction compression of ultrahigh pressure has been employed. (3) The duplex Mg−8Li alloy provides a foundation to elucidate twin-strengthening role by eliminating the influence of secondary precipitates. More attractively, Mg−Li based alloys are also the most lightweight engineering alloy system in existence ($\rho = 1.33-1.65$ g cm^{-3}), for which the impact on enhanced strength can be immense.[23]

Results and Discussion. *Processing and Mechanical Properties.* The total impurity concentration is below 1 wt % (Table S1), which provides a foundation to investigate the role of Li alloying element. Full details of material preparation and procedures are given in the Experimental Section. Briefly, the as-cast material with an equiaxed grain size of ∼200 μm was prepared by vacuum induction melting. Then, the sample with a diameter of 8 mm and a height of 15 mm was used for ultrahigh pressure treatment. The pressure range of 2−6 GPa and the temperature range of 200−1200 °C were engaged. The modified sealed-plug, as shown in the sketch of hexagonal anvil apparatus (Figure S1), was used to avoid melting leakage. Samples are designated as follows: a Mg−8Li alloy with high
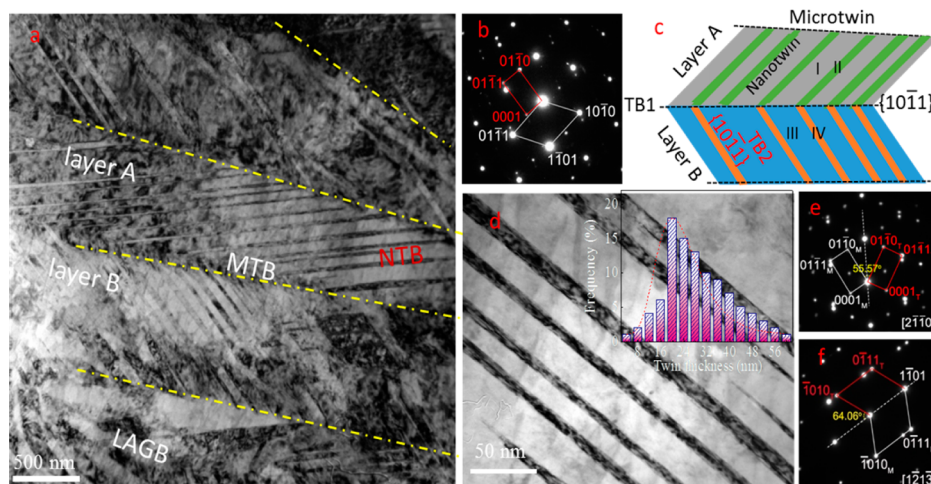
Figure 2. Microstructural characteristics of the 6 GPa−1000 Mg−8Li alloy. (a) Bright field TEM image of the 6 GPa−1000 sample. (b) SAED patterns of LAGB area. (c) Schematic of hierarchical $\{10\bar{1}1\}-\{10\bar{1}1\}$ DCTWs. (d) Enlargement of the $\{10\bar{1}0\}$ NTWs, the inset corresponds to thickness distribution of the $\{10\bar{1}0\}$ NTWs. (e) SAED patterns of NTW interfaces along $[2\bar{1}\bar{1}0]$ direction. (f) SAED patterns of NTW interfaces along $[1\bar{2}1\bar{3}]$ direction.

pressure treatment under 4 GPa at 400 °C will be referred to as a 4 GPa−400 Mg−8Li alloy. The pristine sample of as-cast Mg−8Li alloy is used as a reference.

Figure 1a shows that a volcano-like trend between the microhardness and treated temperatures is observed under a constant pressure during the whole temperature range. The microhardness of the pristine sample is ∼50 HV, and it is increased by over 200% after high pressure treatment (6 GPa, 1000 °C). The peak microhardness is improved by increasing the pressure. The peak value at 6 GPa is ∼108 HV, which is approximately 1.37 times higher than that at 2 GPa. This peak hardness value is the largest one reported until now, which is far higher than those of Mg−Li based alloys after alloying, aging, or severe deformation (Figure S2a). In addition, as exterior pressure increases, the melting points of Mg−8Li alloys increase, and the temperature which reaches the peak value increases correspondingly.

Figure 1b reveals the typical true stress−strain tensile curves of Mg−8Li alloys at different states. Compared with the pristine sample, both yield strength and ultimate tensile strength are improved remarkably, while a high elongation of ∼23.6% remains. Especially, the yield strength of the 6 GPa−1000 Mg−8Li sample (∼249 MPa) is 4.05 times as high as that of the pristine sample. This value is the highest value of Mg−Li based alloys reported so far (Figure 1c). In contrast, the compressive properties were also tested (Figure S2b), in which the same trend is confirmed as tensile testing. The tensile-compression asymmetry is eliminated, and a high compression plasticity remains.

Notably, as shown in Figure 1c, this tensile yield value for the 6 GPa−1000 Mg−8Li sample is not only far higher than those of Mg−Li binary alloys (100 ± 50 MPa) but also higher than those of multiple Mg−Li−X (X: other alloying elements) based alloys, even after different severe plastic deformation treatments, such as rolling,[24] extrusion,[25−27] equal-channel angular pressing (ECAP),[28,29] and aging.[30,31] Additionally, both the specific yield strength and elongation are improved simultaneously in contrast to other commercial Mg or Al alloys (Figure 1d).

Microstructural Characteristics. XRD patterns (Figure S3) show the as-cast sample consists of both body-centered cubic

(bcc) Li-rich phase (β phase) and hcp Mg-rich phase (α phase). For the bcc phase, XRD yields the value of lattice constant, $a = 3.514$ Å. According to the well-resolved hkl (110) reflection, it is established that fine Li precipitate with an average diameter of ∼100 nm is strain-free.[32] Mg peak reflections are slightly displaced attributed to the presence of Li atoms in solid solution. TEM images (Figure S4) show that the circle-shaped precipitates with the diameters ranging from 0.1 to 2 μm are detected in the matrix. The reason for the discrepancy is that XRD patterns reflect an average bulk value, while TEM result generally reflects a local area.

The effect of both pressure and temperature on the microstructure of Mg−8Li alloys has been systematically investigated. By increasing the temperatures, two processes (ultrahigh solid solution and ultrahigh resolidification) sequentially occurred. This trend resembles those high pressure torsion treated results reported in recent works on Cu−Co[33] and Al−Zn alloys.[34,35] The microhardness curve and microstructure variation are similar for all ultrahigh pressure samples. To probe the relationship between phase fraction and microhardness, the phase composition of the Mg−8Li alloys after different high pressure treatments (2, 4, and 6 GPa) has been confirmed by the step-scan method (Figure S5a). The fraction of bcc Li-rich phase and hcp Mg-rich phase has been calculated by Rietveld refinement.[36] The results (Figure S5b) show that the phase fraction of bcc Li-rich phase monotonously decreased in the temperature range of 400−1000 °C. The phase was transformed from bcc Li-rich phase to hcp Li-rich phase in the solid solution range of 400−1000 °C. Additionally, note that the grain size remained at the level of hundred micrometers during the whole ultrahigh pressure treated range (Figure S5b).

2.3. $\{10\bar{1}1\}-\{10\bar{1}1\}$ DCTWs. Two different structures are observed in the bright field TEM image of the 6 GPa−1000 Mg−8Li alloy (Figure 2a). One is the fine band-shaped grains with a low angle grain boundary (∼12 ± 2°, LAGB, Figure 2b), in which no twins are detected. The volume fraction which was calculated based on the TEM image was ∼35%. The other of ∼65% volume fraction is ascribed to a hierarchical double twin structure. Figure 2c illustrates a typical bright field image of two variants, designated A and B, respectively. The thickness of
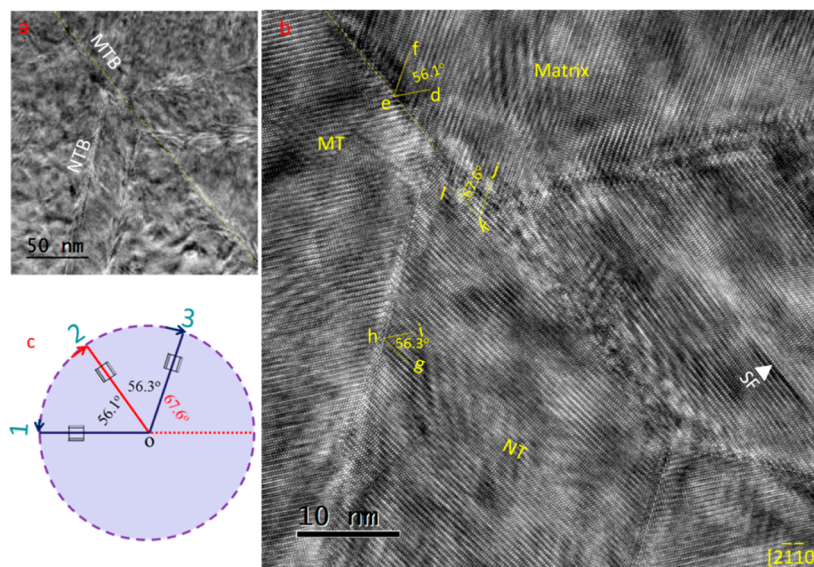
c

Figure 3. Microstructure of $\{10\bar{1}1\}-\{10\bar{1}1\}$ DCTWs. (a) Bright field TEM image of hierarchical $\{10\bar{1}1\}-\{10\bar{1}1\}$ DCTWs in the 6 GPa−1000 Mg−8Li alloy. (b) Local HRTEM image of $\{10\bar{1}1\}-\{10\bar{1}1\}$ DCTWs in panel a. The edge-on MTW interfaces are marked by yellow lines, and the NTW interfaces are shows as white broken lines. (c) Schematic figure shows two possible rotated ways of the *c*-axis in a double twinning process.

macrotwins (MTW) varies in the range of 1−2 μm. A higher magnification image of internal nanotwins (NTW, Figure 2d) demonstrates its volume fraction is ∼10% in the domain of MTW. The average thickness of NTW is ∼20 nm. The SAED pattern in the NTW boundaries (Figure 2e) clearly confirms that the diffracted spots of $\{10\bar{1}1\}_I$ and $\{10\bar{1}1\}_{II}$ are completely overlapped in $\langle 2\bar{1}\bar{1}0 \rangle$ zone axes. Consequently, the orientation relationship (OR) between lamellae I and II in layer A, represented in terms of the parallel directions and planes, is found to be

$$[2\bar{1}\bar{1}0]_I // [2\bar{1}\bar{1}0]_{II} \text{ with } (10\bar{1}1)_I // (10\bar{1}1)_{II}$$

where the subscripts I and II denote the corresponding lamellae. Simultaneously, the SEAD pattern also reveals that the layer I rotates ∼56.41° to overlap with the layer II along the $<2\bar{1}\bar{1}0>$ direction. This is consistent with the common CTW.[13] In addition, noted that the OR between lamellae III and IV in layer B is matching with the experimentally determined OR between lamellae I and II in layer A. According to the above method, the SEAD patter at MTB boundaries was successfully tested. The similar relationship between layer A and B is attained as following:

$$[1\bar{2}13]_A // [1\bar{2}13]_B \text{ with } (1\bar{1}01)_A // (1\bar{1}01)_B$$

The mere difference lies in the different rotation angle 55.57° $\langle 2\bar{1}\bar{1}0 \rangle$. According to calculations based on the Bilby−Crocker theory,[37] the twinning elements are the twinning plane of $(10\bar{1}1)$, the twinning direction of $[10\bar{1}2]$, the reciprocal twinning plane of $(\bar{1}011)$, and the reciprocal twinning plane of $[10\bar{1}2]$. Therefore, it demonstrates that this hierarchical structure of $\{10\bar{1}1\}$-NTW in the interior domain of $\{10\bar{1}1\}$-NTW is a novel $\{10\bar{1}1\}-\{10\bar{1}1\}$ DCTWs.

The HRTEM images (Figure 3a−b) represent the typical junction areas of DCTWs. There are some serrated coherent twin boundaries (Figure S6a). These serrated coherent twin boundaries consist of a large number of sequential $(10\bar{1}1)$ coherent twin boundaries and parallel basal−prismatic planes serrations (BPPS). Notably, some steps with four-atomic-layer are detected in the MTWs boundaries. These steps play a

crucial role in determining the mechanism of twin growth and twin shrinkage because twin boundaries can not continue gliding in the perfect crystal once they meet the steps.[24] NTWs have a great number of stack faults in the interior of twins except for eight atomic-layer steps in the interface, which is related to the deformation[12] (Figure S6b). As shown in Figure 3b, the primary $\{10\bar{1}1\}$-CTW reorients the basal plane by ∼56.1° (∠def) around the $\langle 11\bar{2}0 \rangle$ axis. Then the secondary $\{10\bar{1}1\}$-CTW further rotates the basal plane by ∼56.3°(∠ghi) around the same axis. The net results is a reorientation of the original *c*-axis by ∼67.6°(∠jkl) around the $\langle 11\bar{2}0 \rangle$ axis. Owing to the lowest slip energy on the closed plane,[38] the most probable rotation is related to occur along $\langle 11\bar{2}0 \rangle$ axis. As illustrated in Figure 3c, position 1 denotes the orientation of initial parent grain in the pristine sample. When $\{10\bar{1}1\}$ twinning occurs during radial compression, reorientation by approximately 56° occurs within the plane along $\langle 11\bar{2}0 \rangle$ from 1 to 2 with the highest Schmid factor.[13] During subsequent compression, there are two possible twinning variants for secondary twinning: forward reorientation of the *c*-axis by another 56° following 2 → 3. This is the same twinning variant that occurs during radial compression and reorientation in the reverse direction to original position following 2 → 1. The second variant for secondary twinning is detwinning through the 2 → 1 route will give rise to a complete detwinning trace. For comparison, detwinning through the 2 → 3 route actually proceeds through $\{10\bar{1}1\}-\{10\bar{1}1\}$ detwinning which is accompanied by a transition of twin boundaries (56°) into the interface with misorientation angle of ∼68°. Consequently, two main different morphologies of band-like low angle grains and hierarchical DCTWs are entrapped after high-pressure treatment. This preponderant process is also confirmed by EBSD measurement (Figure S7), wherein the disorientation angle of ∼68 ± 3° dominates the majority of the volume fraction.

Aggregation of hcp-Type Li-Rich Particles in Twin Boundaries. To elucidate the main reason accounting for a dominated $\{10\bar{1}1\}-\{10\bar{1}1\}$ detwinning process, the interface structures of DCTWs were investigated by annular dark-field
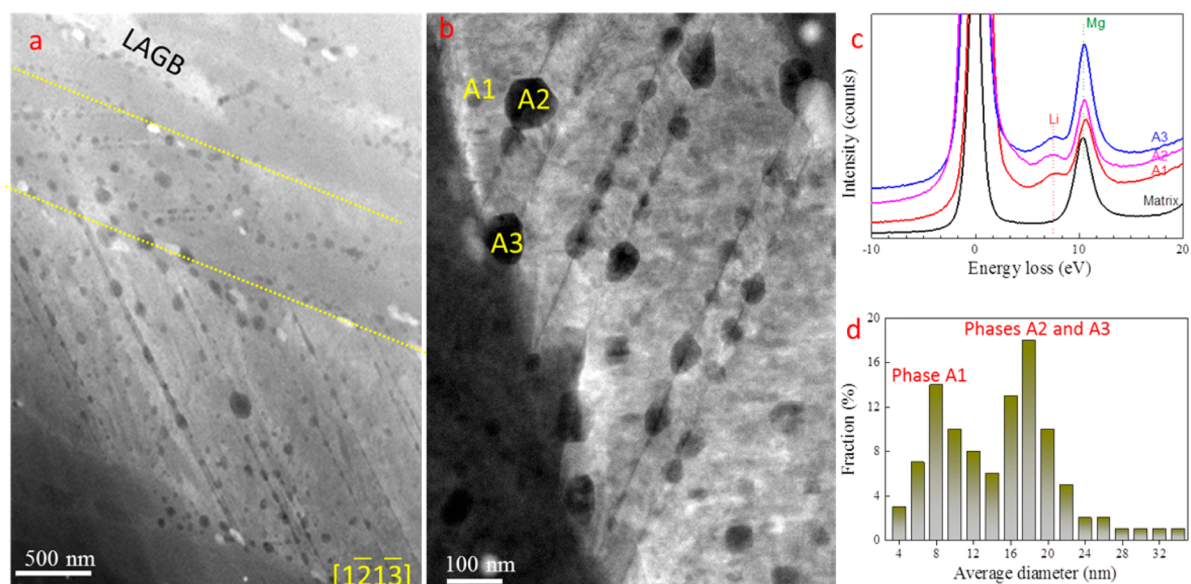
D

Figure 4. Segregation of nanoscaled particles in DCTW boundaries. (a) ADF images of DCTW structure in 6 GPa−1000 Mg−8Li alloy observed along $[1\bar{2}1\bar{3}]$ direction. (b) Local high magnification. (c) EELS maps for different particles. (d) Dimensional distribution of black particles, average 30 random particles were calculated.
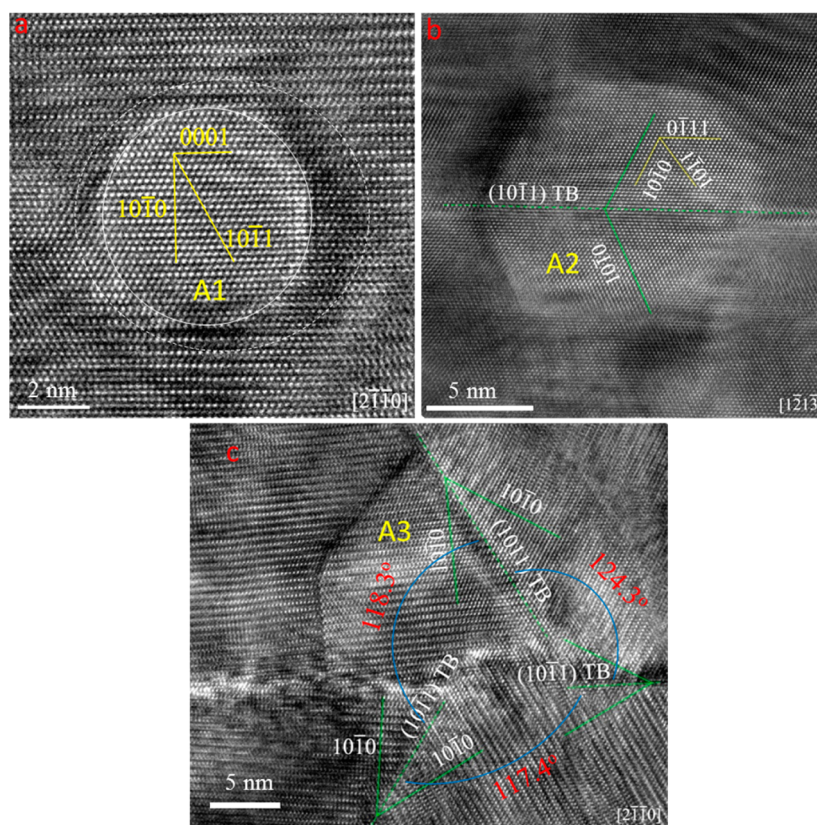

Figure 5. Pinning strengthening of DCTWs boundaries. (a) Coherent nanoscaled hcp Li-rich precipitate in the matrix interior. (b) Coherent growth of hcp Li-rich phase along MTWs boundaries. (c) Segregation of hcp Li-rich phase in the junction area of DCTWs.

(ADF) images and EELS. Figure 4a−b illustrates that there are a large number of particles in DCTWs boundaries along $[1\bar{2}1\bar{3}]$ direction. The element composition was identified by electron energy loss spectroscopy (EELS), which is the most effective approach to distinguish Li and Mg elements. A low voltage of 2 keV and exposed time of 2 s were performed. The results (Figure 4c) show that black particles A1, A2, and A3 are Li-rich

phases. The phase A1 with an average dimension of ∼8 nm (Figure 4d) is mainly distributed in the interior of matrix. Comparatively, the phases A2 and A3 with a dimension of ∼18 nm are segregated along NTW and MTW boundaries as well as the junction area of DCTWs boundaries.

The detailed OR between the particles and the matrix are confirmed by HRTEM (Figure 5). Interestingly, the globular
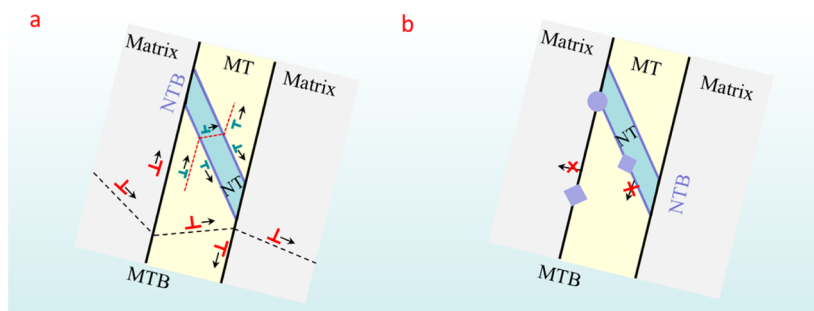
Figure 6. Schematic illustrations of the strengthening mechanism. (a) Two possible strengthening processes by hindering dislocation movement in hierarchical DCTW boundaries. (i) Partial dislocations emitted from GBs travel across other GBs or TBs. (ii) Partial dislocations emitted from TBs travel across TB or GBs. (b) Prevention of two possible softening processes in hierarchical DCTW boundaries-twin interface movement and detwinning. (i) TBs shift together, leading to thickening. (ii) Partial dislocations travel parallel to secondary TBs, resulting in the detwinning of secondary twins.

particle A1 is mainly aligned along the $[2\bar{1}\bar{1}0]$ crystallographic direction. In addition, a typical hcp-structure which is fully coherent with the matrix was further confirmed. Particle A2 symmetrically grows along the NTWs boundaries, which is detected along the $[1\bar{2}1\bar{3}]$ direction. Differing from the particle A1, the dominated facets $\{1\bar{1}01\}$, $\{\bar{1}010\}$, and $\{0\bar{1}11\}$ are confirmed, which is consistent with the Wulff growth model.[39] Finally, note that the three twins with the almost same angle of $\sim120 \pm 5°$ impinge together, resulting the formation of a junction domain. Viewing on the $[2\bar{1}\bar{1}0]$ direction, the whole Li-rich phase is divided into three parts. In every subarea, the Li-rich particles show the coherent crystalline lattice within the matrix. The preferential position of different particles is closely related to the structure of twin boundaries.[40,41]

Strengthening Mechanisms. The yield strength of pristine Mg−8Li alloy with a grain dimension of hundred micrometers is very low (~55 MPa), and the main strengthening mechanism is related to solid solution strengthening. In contrast, the yield strength is significantly improved, which is 4.05 times as high as that of the pristine sample. Simultaneously, a high elongation to fraction remains. Taking into account the similar grain size, this improved yield value is mainly attributed to unique microstructures: hierarchical DCTWs and fine nanosized hcp-type Li-rich phases. Furthermore, this is confirmed by a large number of dislocations accumulating along DCTWs boundaries and particles during deformation (Figure S8).

Figure 6a shows the deformation mechanisms of hierarchical DCTWs are dominated by the following two Hall−Petch type strengthening mechanisms:[42,43] (i) partial dislocations emitted from GBs travel across other GBs or TBs and (ii) partial dislocations emitted from TBs travel across TB or GBs. Provided that the width of twin corresponds to the grain size, the twin strengthening role will be estimated based on the similarity as grain refining strengthening, in terms of eq 1:[43,44]

$$\Delta\sigma = m_1 k \lambda_1^{-1/2} + m_2 k \lambda_2^{-1/2} \tag{1}$$

where λ_1 and λ_2 are the average width of MT and NT, respectively; k is the Hall Petch constant, m_1 and m_2 are the volume fractions. According to the parameters in Table S2, the increment of yield strength by introducing hierarchical twins is ~154 MPa.

The hierarchical twins exist simultaneously two possible softening mechanisms.[34] As illustrated in Figure 6b, TBs shift together and lead to vary twin width. In addition, partial dislocations travel parallel to secondary TBs, resulting in the detwinning of secondary twins. Fortunately, some fine coherent

hcp-type Li-rich particles (Figure 4a) are formed in these TBs at ultrahigh pressure. The nanosized particles bestows two merits:[45,46] the presence of precipitates contributes to the formation of serrated boundaries due to one side of TB being stabilized by the precipitate, which effectively hinds dislocation motion along TBs. Additionally, the nanosized particles can decrease the dislocation to pass through TB interface, prohibiting the widening of TBs. This TB motion is impeded by the Orowan stress required for twinning dislocation bowing around the precipitates by eq 2:[47,48]

$$\sigma_o = m_2 \frac{MGb}{2\pi\sqrt{1-\nu}}\left(\frac{1}{\tau}\right)\ln\left(\frac{d}{r}\right) \tag{2}$$

where σ_o is the increase in CRSS for twinning dislocations due to nanoscale Li-rich precipitate strengthening, where M is the Taylor factor, G is the shear modulus, b is the Burger vector of the dislocation; ν is Poissons ratio; τ is the effective interparticle spacing on twin plane, d is the mean planar diameter of the particles on the twin plane, and r is the inner cutoff radius of the dislocation taken equal to b and m for the volume fraction. The τ lies in the range of 5−30 nm, and the increased CRSS value corresponds to 13−78 MPa. It is higher than that of stress required to move dislocations parallel to the TBs (5−10 MPa).

In fact, the effect of precipitates on twinning is complicated by the fact that the plastic relaxation processes will depend on the long-range internal stresses in the matrix caused by the interaction of both twinning and slip dislocations with the particles. Except for the several main roles mentioned above, the serrated interface and fine stacking faults in the interior of NTW domain will provide further obstacles to the passage of twinning dislocations.[49] Unfortunately, the quantitative contribution is impossible owing to the absence of suitable model so far. It will be discussed in detail elsewhere in future.

Conclusions. In summary, we have reported a novel strategy for evading the strength−ductility trade-off dilemma in Mg alloys through gradient hierarchical new and fine double contraction nanotwins by a one-step ultrahigh pressure procedure. A conventional cocoon, in which it was impossible to strengthen Mg alloys by twin structure owing to its unstable twin interface and stress concentration at the tip of twin, has been successfully overcome. Differing from traditional strengthening methods, such as grain refining and precipitate strengthening, the formation of staggered twins can effectively prohibit dislocation motion. Concurrently, the new nanoscaled hcp-type Li-rich phase first reported not only overcomes the

thickening of twin interface but also prohibits the dislocation slip along twin boundaries.

Experimental Section. *Sample Preparation.* The alloy with the nominal composition of Mg−8 wt % Li was utilized to carry out the experiments. The cast bar with a diameter of 30 mm was prepared by high pure raw materials in an electromagnetic induction melting furnace under the argon gas atmosphere. The chemical composition of the as-cast samples was analyzed by inductively coupled plasma atomic emission spectroscopy (ICP-AES). The cast bar was machined into cylindrical specimens with a diameter of 10 mm and a length of 14 mm for ultrahigh pressure treatment in a modified CS-IB type hexahedral anvil apparatus. First, the sample was wrapped with tantalum foil and, subsequently, inserted in a BN capsule which was thermally stable. The samples were heated in a graphite furnace, and a cubic pyrophyllite filled the role of the pressure medium. The hydrostatic-high pressure could be obtained by the press along the three axes. The samples were treated for 30 min at temperatures from room temperature (RT) to 1200 °C under high pressures of 2, 4, and 6 GPa. After ultrahigh pressure treatment, the samples were quenched to room temperature directly before unloading pressure.

Mechanical Properties. Microhardness was measured in a FM-ARS-9000 Vickers hardness tester. The test load and loading times are 200 g and 10 s, respectively. The average hardness has been calculated using the dependence of 5×5 matrix measures. Mechanical tests were performed on a Gleeble-3500 thermomechanical simulator at a strain rate of 1.7×10^{-3} s^{-1}. Compressive samples were cylinder shaped with the diameter and length of 8 and 12 mm, respectively. At least five parallel samples were tested to obtain the average values. Dog-bone tensile test samples with a gauge of 6 mm were used in tensile tests. The value was averaged over at least three measurements.

Microstructural Characterization. The microstructural investigations were performed using an optical microscopy and SEM. Samples for OM and scanning electron microscope (SEM) were prepared by a procedure involving grinding up to 2400 SiC paper, followed by mechanical polishing with 9, 3, and 1 μm water-free diamond suspensions and final polishing using 0.05 μm colloidal silica. The final step included chemical polishing in a fresh solution containing a mixture of 100 mL of methanol, 12 mL of hydrochloric acid, and 8 mL of nitric acid. XRD was carried out on the Rigatu D/MAX/2500/PC with Cu Kα radiation at a scan from 30° to 70° with a step of 0.02 and a permanence time of 2 s. The XRD results were analyzed by means of Rietveld refinement (using the software Rietica).

To reveal the evolution of microstructure and twin during the high-pressure treatment processing, electron backscatter diffraction (EBSD) analyses were conducted on a SEM equipped with a HKL-EBSD system. The samples for EBSD mapping were mechanically ground and electrochemically polished in the AC2 electrolyte. EBSD data were analyzed using the Channel 5 software. A step size of 0.5 μm was employed for EBSD mapping. Thin foil specimens of 3 mm in diameter were punched from the slices for transmission electron microscopy (TEM) observation. The samples were prepared by mechanical polishing from 500 μm to ∼30 μm in thickness and then ion-beam milling using Gatan PIPS 691 with 4 keV. Conventional TEM observations were conducted using a JEM-2010 TEM operated at a voltage of 200 kV and recorded by a Gatan model-794 CCD digital camera. In addition, the nanoscaled phase, twin microstructure, and elemental compo-

sition of the same specimens were identified by high-resolution transmission electron microscopy [HRTEM, FEI TITAN ETEM G2: a ultrahigh point resolution of 0.1 nm with a Gatan model-994 CCD digital camera and an electron energy loss spectrometer (EELS), operated at a voltage of 300 kV].

■ AUTHOR INFORMATION

Corresponding Author

*E-mail: pengqiuming@gmail.com.

ORCID

Qiuming Peng: 0000-0002-3053-7066

Notes

The authors declare no competing financial interest.

■ REFERENCES

(1) Kainer, K. U. *Magnesium Alloys and their Applications*; Wiley-VCH, 1999.

(2) Friedrich, H. E.; Mordike, B. L. *Magnesium Technology (Metallurgy, Design Data, Applications)*; Springer-Verlag, 2006.

(3) Pan, F.; Yang, M.; Chen, X. *J. Mater. Sci. Technol.* **2016**, *32*, 1211−1221.

(4) Yuan, T.; Luo, Z.; Kou, S. *Acta Mater.* **2016**, *116*, 166−176.

(5) Chen, L. Y.; Xu, J. Q.; Choi, H.; Pozuelo, M.; Ma, X.; Bhowmick, S.; Yang, J. M.; Mathaudhu, S.; Li, X. C. *Nature* **2015**, *528*, 539−543.

(6) Westengen, H.; Khalfalla, Y.; Benyounis, K. Y. *Reference Module in Materials Science and Materials Engineering*; Elsevier, 2016.

(7) Yu, Q.; Qi, L.; Chen, K.; Mishra, R. K.; Li, J.; Minor, A. M. *Nano Lett.* **2012**, *12*, 887−892.

(8) Huang, Q.; Yu, D.; Xu, B.; Hu, W.; Ma, Y.; Wang, Y.; Zhao, Z.; Wen, B.; He, J.; Liu, Z.; Tian, Y. *Nature* **2014**, *510*, 250−253.

(9) Tian, Y.; Xu, B.; Yu, D.; Ma, Y.; Wang, Y.; Jiang, Y.; Hu, W.; Tang, C.; Gao, Y.; Luo, K.; Zhao, Z.; Wang, L. M.; Wen, B.; He, J.; Liu, Z. *Nature* **2013**, *493*, 385−388.

(10) Nie, J. F.; Zhu, Y. M.; Liu, J. Z.; Fang, X. Y. *Science* **2013**, *340*, 957−960.

(11) Wei, Y.; Li, Y.; Zhu, L.; Liu, Y.; Lei, X.; Wang, G.; Wu, Y.; Mi, Z.; Liu, J.; Wang, H.; Gao, H. *Nat. Commun.* **2014**, *5*, 3580.

(12) Lu, K.; Lu, L.; Suresh, S. *Science* **2009**, *324*, 349−352.

(13) Barnett, M. R. *Mater. Sci. Eng., A* **2007**, *464*, 8−16.

(14) Barnett, M. R. *Mater. Sci. Eng., A* **2007**, *464*, 1−7.

(15) Mu, S.; Jonas, J. J.; Gottstein, G. *Acta Mater.* **2012**, *60*, 2043−2053.

(16) Christian, J. W.; Mahajan, S. *Prog. Mater. Sci.* **1995**, *39*, 1−157.

(17) Cizek, P.; Barnett, M. R. *Scr. Mater.* **2008**, *59*, 959−962.

(18) Lentz, M.; Risse, M.; Schaefer, N.; Reimers, W.; Beyerlein, I. J. *Nat. Commun.* **2016**, *7*, 11068.

(19) Chun, J. S.; Byrne, J. G.; Bornemann, A. *Philos. Mag.* **1969**, *20*, 291−300.

(20) Lu, L.; Shen, Y.; Chen, X.; Qian, L.; Lu, K. *Science* **2004**, *304*, 422−426.

(21) Wang, H.; Clausen, B.; Capolungo, L.; Beyerlein, I. J.; Wang, J.; Tomé, C. N. *Int. J. Plast.* **2016**, *79*, 275−292.

(22) Agnew, S. R.; Yoo, M. H.; Tomé, C. N. *Acta Mater.* **2001**, *49*, 4277−4289.

(23) Xu, W.; Birbilis, N.; Sha, G.; Wang, Y.; Daniels, J. E.; Xiao, Y.; Ferry, M. *Nat. Mater.* **2015**, *14*, 1229−1235.

(24) Kim, J.; Jeong, H. J.; Moon, Y.; Kim, K. B.; Son, H. T.; Jeon, C.; Sim, J. W.; Moon, S.; Park, J. M. *J. Alloys Compd.* **2017**, *711*, 243−249.

(25) Kim, J. T.; Park, G. H.; Kim, Y. S.; Hong, S. H.; Park, H. J.; Suh, J. Y.; Son, H. T.; Lee, M. H.; Park, J. M.; Kim, K. B. *J. Alloys Compd.* **2016**, *687*, 821−826.

(26) Jiang, B.; Zeng, Y.; Zhang, M.; Yin, H.; Yang, Q.; Pan, F. *Trans. Nonferrous Met. Soc. China* **2013**, *23*, 904−908.

(27) Zhang, J.; Zhang, L.; Leng, Z.; Liu, S.; Wu, R.; Zhang, M. *Scr. Mater.* **2013**, *68*, 675−678.

(28) Karami, M.; Mahmudi, R. *Mater. Sci. Eng., A* **2014**, *607*, 512−520.

(29) Karami, M.; Mahmudi, R. *Mater. Sci. Eng., A* **2013**, *576*, 156−159.

(30) Wu, R.; Zhang, M. *Mater. Sci. Eng., A* **2009**, *520*, 36−39.

(31) Qu, Z.; Wu, R.; Zhan, H.; Zhang, M. *J. Alloys Compd.* **2012**, *536*, 145−149.

(32) Zhang, L.; Li, S. *Phys. B* **2014**, *434*, 38−43.

(33) Bachmaier, A.; Schmauch, J.; Aboulfadl, H.; Verch, A.; Motz, C. *Acta Mater.* **2016**, *115*, 333−346.

(34) Cho, T. S.; Lee, H. J.; Ahn, B.; Kawasaki, M.; Langdon, T. G. *Acta Mater.* **2014**, *72*, 67−79.

(35) Borodachenkova, M.; Barlat, F.; Wen, W.; Bastos, A.; Grácio, J. J. *Int. J. Plast.* **2015**, *68*, 150−163.

(36) Von Dreele, R. B.; Jorgensen, J. D.; Windsor, C. G. *J. Appl. Crystallogr.* **1982**, *15*, 581−589.

(37) Crocker, A. G.; Bilby, B. A. *Acta Metall.* **1961**, *9*, 678−688.

(38) Clausen, B.; Tomé, C. N.; Brown, D. W.; Agnew, S. R. *Acta Mater.* **2008**, *56*, 2456−2468.

(39) Marks, L. D. *J. Cryst. Growth* **1983**, *61*, 556−566.

(40) Leclercq, L.; Capolungo, L.; Rodney, D. *Mater. Res. Lett.* **2014**, *2*, 152−159.

(41) Wang, J.; Liu, L.; Tomé, C. N.; Mao, S. X.; Gong, S. K. *Mater. Res. Lett.* **2013**, *1*, 81−88.

(42) Yuan, F.; Wu, X. *J. Appl. Phys.* **2013**, *113*, 203516.

(43) Zhu, L.; Kou, H.; Lu, J. *Appl. Phys. Lett.* **2012**, *101*, 081906.

(44) Zhang, Z.; Sheng, H.; Wang, Z.; Gludovatz, B.; Zhang, Z.; George, E. P.; Yu, Q.; Mao, S. X.; Ritchie, R. O. *Nat. Commun.* **2017**, *8*, 14390.

(45) Huang, C. X.; Hu, W. P.; Wang, Q. Y.; Wang, C.; Yang, G.; Zhu, Y. T. *Mater. Res. Lett.* **2015**, *3*, 88−94.

(46) Wu, X. L.; Jiang, P.; Chen, L.; Zhang, J. F.; Yuan, F. P.; Zhu, Y. T. *Mater. Res. Lett.* **2014**, *2*, 185−191.

(47) Zhang, Z.; Chen, D. L. *Scr. Mater.* **2006**, *54*, 1321−1326.

(48) Queyreau, S.; Monnet, G.; Devincre, B. *Acta Mater.* **2010**, *58*, 5586−5595.

(49) Yu, Q.; Wang, J.; Jiang, Y.; McCabe, R. J.; Li, N.; Tomé, C. N. *Acta Mater.* **2014**, *77*, 28−42.